7 Plasmonics

Highlights of this chapter: In this chapter we introduce the concept of surface plasmon polaritons (SPP). We discuss various types of SPP and explain excitation methods. Finally, different recent research topics and applications related to SPP are introduced.

7.1 Introduction

Long before scientists have started to investigate the optical properties of metal nanostructures, they have been used by artists to generate brilliant colors in glass artefacts and artwork, where the inclusion of gold nanoparticles of different size into the glass creates a multitude of colors. Famous examples are the Lycurgus cup (Roman empire, 4th century AD), which has a green color when observing in reflecting light, while it shines in red in transmitting light conditions, and church window glasses.

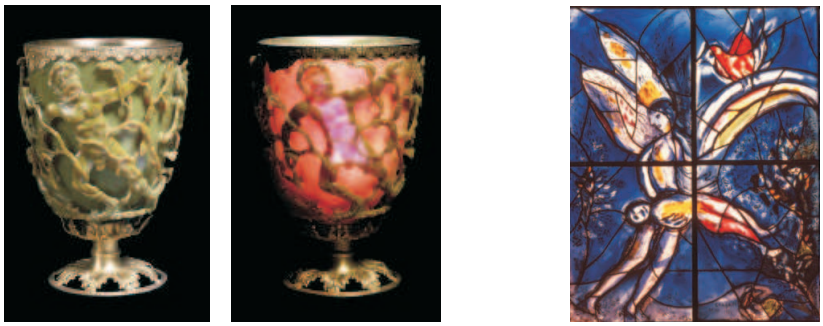

Figure 172: Left: Lycurgus cup, right: color windows made by Marc Chagall, St. Stephans Church in Mainz

Today, the electromagnetic properties of metal–dielectric interfaces undergo a steadily increasing interest in science, dating back in the works of Gustav Mie (1908) and Rufus Ritchie (1957) on small metal particles and flat surfaces. This is further motivated by the development of improved nano-fabrication techniques, such as electron beam lithographie or ion beam milling, and by modern characterization techniques, such as near field microscopy. Todays applications of surface plasmonics include the utilization of metal nanostructures used as nano-antennas for optical probes in biology and chemistry, the implementation of sub-wavelength waveguides, or the development of efficient solar cells.

7.2 Electro-magnetics in metals and on metal surfaces

7.2.1 Basics

The interaction of metals with electro-magnetic fields can be completely described within the frame of classical Maxwell equations:

$$\nabla \cdot \mathbf{D} = \rho \tag{316}$$
$$\nabla \cdot \mathbf{B} = 0 \tag{317}$$
$$\nabla \times \mathbf{E} = -\partial \mathbf{B}/\partial t \tag{318}$$
$$\nabla \times \mathbf{H} = \mathbf{J} + \partial \mathbf{D}/\partial t, \tag{319}$$

which connects the macroscopic fields (dielectric displacement $\mathbf{D}$, electric field $\mathbf{E}$, magnetic field $\mathbf{H}$ and magnetic induction $\mathbf{B}$) with an external charge density ρ and current density $\mathbf{J}$.

In the limit of linear, isotropic and non-magnetic media, there are additionally the material dependent relations:

$$\mathbf{D} = \epsilon_0 \epsilon \mathbf{E} \tag{320}$$
$$\mathbf{B} = \mu_0 \mathbf{H} \tag{321}$$

with a frequency dependent dielectric constant: $\epsilon = \epsilon(\omega)$, which is in general a complex function, $\epsilon = \epsilon' + i\epsilon''$. It is furthermore connected to the complex index of refraction via $n = n + i\kappa = \sqrt{\epsilon}$. Explicitly one can obtain the following expressions:

$$\epsilon' = n^2 - \kappa^2, \qquad \epsilon'' = 2n\kappa, \tag{322}$$
$$n^2 = \frac{\epsilon'}{2} + \frac{1}{2}\sqrt{\epsilon'^2 + \epsilon''^2}, \qquad \kappa = \frac{\epsilon''}{2n} \tag{323}$$

The real part of the refractive index $n(\omega)$ is responsible for the dispersion in the medium, the imaginary part $\kappa(\omega)$ (extinction coefficient) determines the absorption. Beer's law describes the exponential decay of the intensity of a light beam (along the x direction) in a medium: $I(x) = I_0 \exp(-\alpha x)$. The absorption constant can then be determined from the extinction coefficient: $\alpha(\omega) = 2\kappa(\omega)\omega/c$.

7.2.2 Bulk plasmons

The optical properties can be described over a large frequency range using the *plasma model*, where an electron gas (effective electron mass M) of density N is assumed that freely propagates behind a background of positively charged atom

cores. These electrons start to oscillate in the presence of an electromagnetic field $\mathbf{E}(\mathbf{t}) = \mathbf{E}_0 \exp(-i\omega t)$ and are damped through collisions with a characteristic rate $\gamma = 1/\tau$ (typically $\tau \approx 10^{-14}$ s at room temperature). The equations of motion in this model are

$$m\ddot{\mathbf{x}} + m\gamma\dot{\mathbf{x}} = -e\mathbf{E}(\mathbf{t})$$

with the solution

$$\mathbf{x}(\mathbf{t}) = \frac{e}{m(\omega^2 + i\gamma\omega)}\mathbf{E}(\mathbf{t})$$

The electrons which are displaced relative to the atom cores then generate a polarisation $\mathbf{P} = -Ne\mathbf{x}$. From this it follows for the dielectric displacement and the dielectric constant:

$$\begin{aligned} \mathbf{D} &= \epsilon_0\mathbf{E} + \mathbf{P} = \epsilon_0\epsilon\mathbf{E} && (324)\\ &= \epsilon_0\left(1 - \frac{\omega_p^2}{\omega^2 + i\gamma\omega}\right)\mathbf{E} && (325)\\ \Rightarrow \epsilon(\omega) &= 1 - \frac{\omega_p^2}{\omega^2 + i\gamma\omega} = 1 - \frac{\omega_p^2\tau^2}{\omega^2\tau^2 + i\omega\tau}, && (326) \end{aligned}$$

where we introduced the *plasmon frequency* $\omega_p^2 = Ne^2/(\epsilon_0 m)$.

In case of low frequencies $\kappa\tau \ll 1$ metals are strongly absorbing. The absorption constant then becomes $\alpha = \sqrt{2\omega_p^2\omega\tau/c^2}$. The penetration depth of the fields at low frequencies after Beer's law becomes $\delta = 2/\alpha$ and is called skin depth.

However at large frequencies the approximation $\omega\tau \gg 1$ is valid. In this case the damping term $i\omega\tau$ can be neglected and $\epsilon(\omega)$ becomes approximately real:

$$\epsilon(\omega) = 1 - \frac{\omega_p^2}{\omega^2} \tag{327}$$

The dispersion relation of electro-magnetic fields can be determined from $k^2 = |\mathbf{k}|^2 = \epsilon\omega^2/c^2$:

$$\omega(k) = \sqrt{\omega_p^2 + k^2/c^2}$$

As can be also seen in the figure 173, there is no propagation of electro-magnetic waves below the plasmon frequency $\omega < \omega_p$. For $\omega > \omega_p$ waves propagate with a group velocity $v_g = d\omega/dk < c$.

Of further interest is the special case $\omega = \omega_p$, where for low damping $\epsilon(\omega_p) = 0$. One can show (see e.g. S. Maier: "'Plasmonics"', p. 10 & 15f), that here a

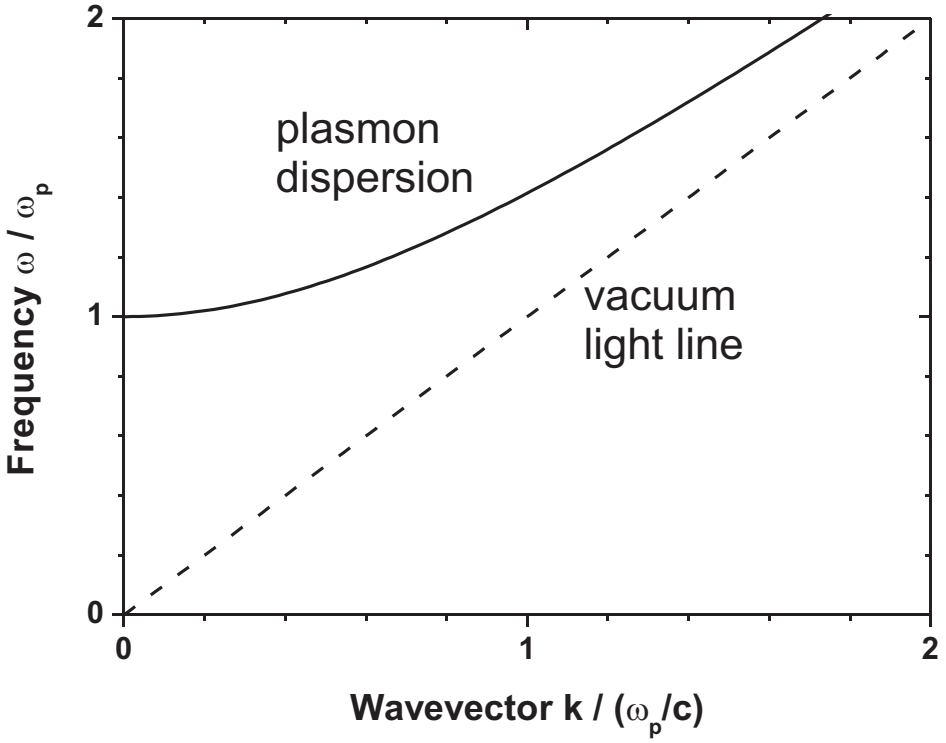

Figure 173: Dispersion relation of the free electron gas.

collective longitudinal excitation mode ($\mathbf{k} \parallel \mathbf{E}$) is formed, with a purely de-polarizing field ($\mathbf{E} = (-1/\epsilon_0)\mathbf{P}$). The physical interpretation is a collective oscillation of the conduction electron gas with respect to the fixed background of positive atom cores. The quanta of this charge oscillation are called *plasmons* (or *bulk plasmons*, for better discrimination with *surface plasmons* in the later sections). As these are longitudinal waves, bulk plasmons cannot couple to transversal electro-magnetic fields and thus cannot be excited from or strayed to direct irradiation.

In most metals, the plasma frequency is in the ultra-violet regime, with energies within 5-15 eV, depending on the metal band structure.

7.2.3 Surface plasmons

Surface plasmons (or more exactly surface plasmon polaritons, SPPs) are electromagnetic excitations that propagate along the interface between a metal and a dielectric medium.

For the derivation of these excitation we again start with Maxwell's equations, which have to be separately solved for the metal and dielectric parts. Let us first start with a metal surface that extends infinitely in the x–y plane at $z = 0$ (see figure 174)

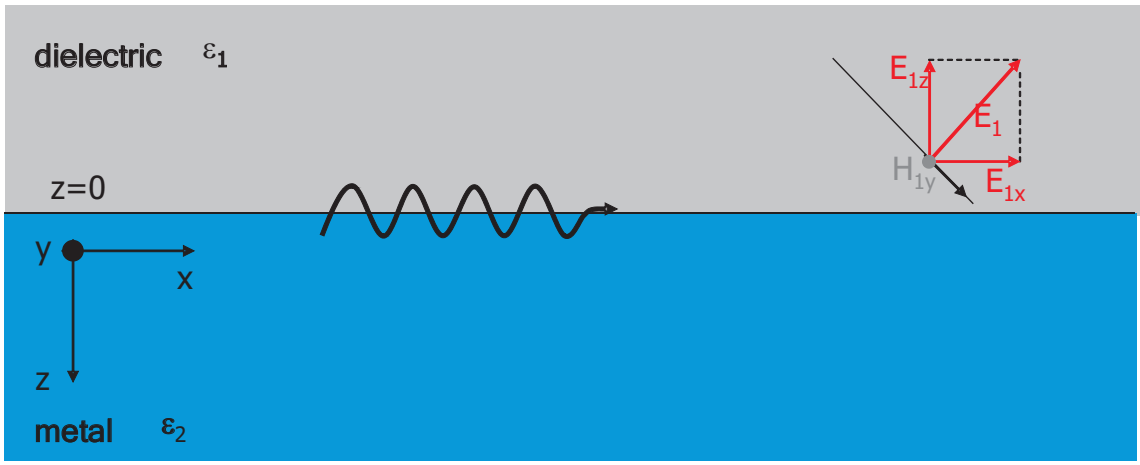

Figure 174: interface along the x–y plane between a dielectric (top, index 1), and a metal (bottom, index 2).

The conditions for the continuity of the normal and transversal field components on this interface (see e.g. J.D. Jackson, "'Classical Electrodynamics"') are given by:

$$D_{1,z} = D_{2z}, \qquad B_{1,z} = B_{2,z} \tag{328}$$

$$E_{1,x/y} = E_{2x/y}, \qquad H_{1,x/y} = H_{2,x/y} \tag{329}$$

where the indices (1) and (2) indicate the dielectric and metal, respectively.

One can show (see e.g. S. Maier: "'Plasmonics"', S. 26f), that under these conditions, no transverse-electric (TE) modes can exist. Instead we directly start with an ansatz for a transverse-magnetic (TM) mode for field which propagate along the

x direction ($i = 1, 2$):

$$\mathbf{E}_i = (E_{i,x}, 0, E_{i,y}) e^{i(\mathbf{k}_i \cdot \mathbf{r} - i\omega t)} \tag{330}$$

$$\mathbf{H}_i = (0, H_{i,y}, 0) e^{i(\mathbf{k} \cdot \mathbf{r} - i\omega t)} \tag{331}$$

$$\mathbf{D}_i = \epsilon_0 \epsilon_i \mathbf{E}_i, \qquad \mathbf{B}_i = \mu_0 \mathbf{H}_i \tag{332}$$

The wave vector is given by $\mathbf{k}_i = (\beta, 0, k_{i,z})$, where $\beta = k_x$ indicates the propagation constant along x.

Using this approach with the conditions of continuity from above and the Maxwell's equation (316) and (319) in absence of charges and currents ($\rho = 0$, $\mathbf{J} = 0$), we obtain the following relations between the $k_{i,z}$ components:

$$\frac{k_{1,z}}{\epsilon_1} = \frac{k_{2,z}}{\epsilon_2} \tag{333}$$

We are looking for solutions that describe modes bound to the interface. Thus, the $k_{i,z}$ components have to be imaginary and of opposite sign:

$$k_{1,z} = +i\kappa_1$$

In this way, the fields decay exponentially into the respective half spaces: $\mathbf{E}_i \propto \exp(\pm i k_{i,z}) = \exp(\pm \kappa_i z)$, as also symbolized in figure 175. Comparing this with the relation (333), one can directly see that this is fulfilled only, if the dielectric constants of the two materials are of opposite sign (i.e. $\epsilon_1 = -\epsilon_2$). Surface plasmons can thus indeed only exist at the interface between a metal ($\epsilon < 0$) and a dielectric medium ($\epsilon > 0$).

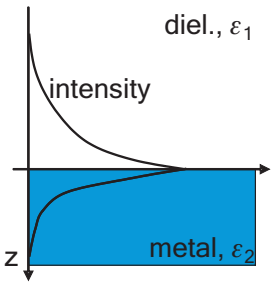

Figure 175: Evanescent field that decays exponentially into the two half spaces.

Altogether, one obtains a system that is composed of an electro-magnetic wave in the dielectric medium and an oscillating electron plasma in the metal, where

both modes have an exponentially decaying evanescent character (see figure 176). Due to this composed character, surface plasmons are also referred to as surface plasmon *polaritons*. The penetration depth of the field into the dielectric is typically on the order of $\lambda/2$ of the wavelength in the medium, whereas in the metal it is characteristically given by the skin depth.

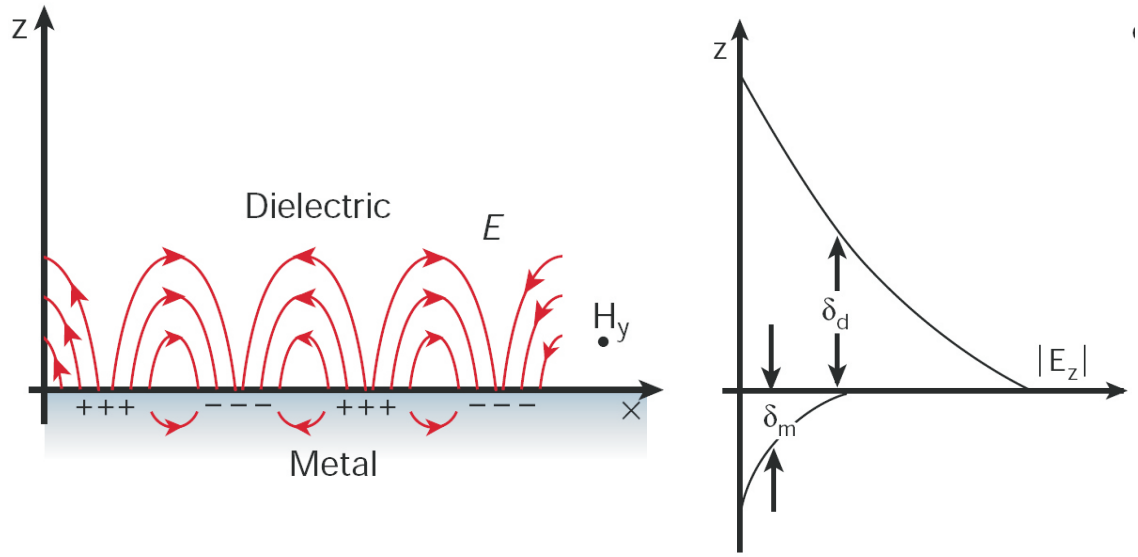

Figure 176: Left: composed character of SPPs at the interface between dielectric and metal. Right: evanescent fields in the two half spaces. [From Barnes et al., Nature 424, 824]

Let us now derive the dispersion relations for surface plasmons. For the wave vector from eq. (330) we get:

$$|\mathbf{k}_{1(2)}|^2 = \epsilon_{1(2)} k_0^2 = \beta^2 + k_{1(2),z}^2 = \beta^2 - \kappa_{1(2)}^2$$

here, $k_0 = \omega/c$ is the vacuum wave vector of light with frequency ω. Insertion of $\kappa_{1(2)}$ into eq. (333) yields the propagation constant:

$$\beta = \frac{\omega}{c} \sqrt{\frac{\epsilon_1 \epsilon_2}{\epsilon_1 + \epsilon_2}} \tag{334}$$

Together with the information of the frequency dependence of $\epsilon_{1(2)}(\omega)$, one can derive for the dispersion relation $\omega(k_{SPP})$.

Under the assumption that $\epsilon_1(\omega)$ in the dielectric is approximately constant and using the approximation (327) for ϵ_2 in the metal above the plasmon frequency, one obtains a dispersion relation as given in figure 177.

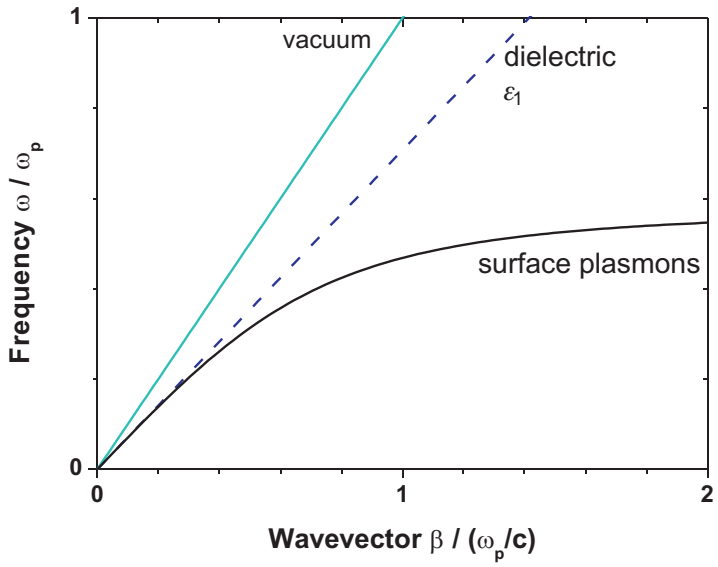

Figure 177: Dispersion relation of surface plasmons compared to light in vacuum and in the dielectric medium.

One realizes that the SPP dispersion relation completely resides below the light cones, while a crossing only occurs in the limit $\omega = 0$, $\beta = 0$. SPPs thus cannot be excited by direct illumination of light, as energy and momentum conservation ($\omega_{\text{light}} = \omega_{SPP}$ and $\mathbf{k}_{\text{light}} = \mathbf{k}_{SPP}$) can not be fulfilled at the same time. Instead, in order to excite SPPs, a momentum transfer has to be established. Techniques to achieve this will be discussed in the next chapter.

In the above discussion we have not yet considered the complex nature of the dielectric constant of metal. Figure 178 shows the real and imaginary part of the dielectric constant for some selected metals. The imaginary part of the dielectric constant causes Ohmic damping of the electrons oscillations in the metal. When using eq. (334), one sees that the propagation constant also becomes imaginary, $\beta = \beta' + i\beta''$. As a consequence, in the solutions for the SPPs, eq. (330), an exponentially decaying damping term $\exp(-\beta'' x)$, which leads to a characteristic

propagation length of SPPs is given by

$$\delta_{SP} = \frac{1}{2\mathrm{Im}(\beta)}$$

These typically range within a few micrometers at visible wavelength and up to 100μm in the infrared.

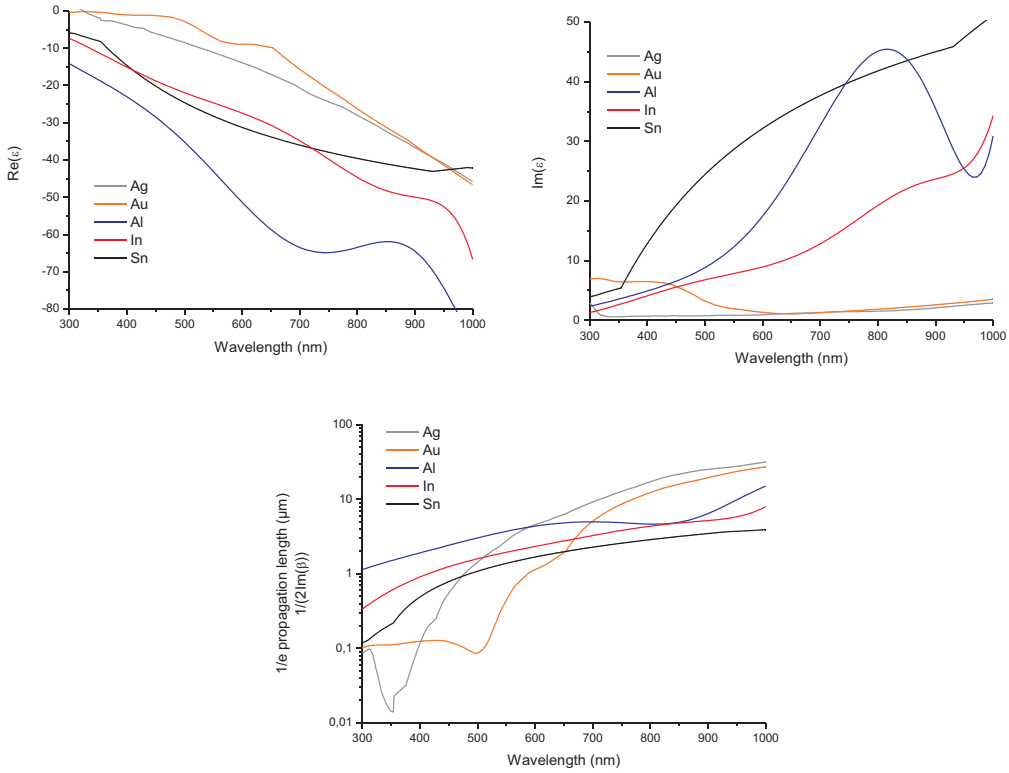

Figure 178: Real (left) and imaginary (right) part of the dielectric constant for some selected metals. Bottom: propagation lengths.

This situation becomes different in case of metal films (thickness d) with two interfaces to dielectric substrates. In the case of a thick metal film on a dielectric substrate two independent SPP modes exist related to different dielectric constants of the media adjacent to metal interfaces. These modes will degenerate if the film

is in a symmetrical environment. If a metal film is thin enough so that the electromagnetic interaction between the interfaces cannot be neglected, the SPP dispersion is significantly modified and coupling between SPP modes on different interfaces of the film must be considered. The interaction of SPP modes removes the degeneracy of the spectrum and the surface plasmon frequencies split into two branches corresponding to symmetric (low-frequency mode) and antisymmetric (high-frequency mode) field distributions through the film. For large SPP wavevectors these modes can be estimated from

$$\omega_{\pm} = \omega_{SP}\sqrt{1 \pm \exp(-\beta d)}$$

At the same time, for such thin metal films, the imaginary part of the wavevector determining the propagation length of high-frequency SPP modes decreases as d^2 with the film thickness. This leads to a very long propagation length of such SPP modes, called the *long-range SPPs*. These modes can have propagation lengths up to centimeters in the infrared regime.

7.3 Excitation of surface plasmon polaritons

As shown in the previous section, the SPP dispersion curve lies entirely below that of free space light in the dielectric, such that $\beta > k$. Direct excitation of SPPs by light beams is thus not possible unless special techniques to achieve phase matching are employed. These will be discussed in this chapter.

7.3.1 Prism coupling

This coupling scheme, also known as attenuated total internal reflection, involves the coupling of the SPPs to the evanescent electro-magnetic field that is formed upon total internal reflection of a light beam at a surface in an optically dense medium. Two different geometries for prism coupling are possible, see figure 179.

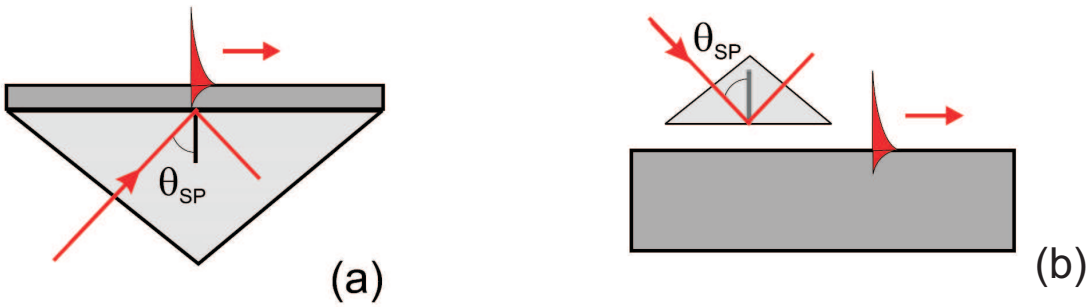

Figure 179: Prism coupling: (a) Kretschmann, (b) Otto configuration. [From Zayats and Smolyaninov, J. Opt. A: Pure Appl. Opt. 5 (2003) S16S50]

In the Kretschmann configuration, the metal film is evaporated on top of a glass prism. The film is illuminated through the dielectric prism at an angle of incidence greater than the angle of total internal reflection. The wavevector of light is increased in the optically dense medium. At a certain angle θ of incidence where the in-plane component of the photon wavevector in the prism coincides with the SPP wavevector on an air–metal surface, resonant light tunnelling through the metal film occurs and light is coupled to the surface polaritons:

$$\beta = \frac{\omega}{c}\sqrt{\epsilon_{\text{prism}}}\sin\theta$$

Under these resonant conditions, a sharp minimum is observed in the reflectivity from the prism interface as light can be coupled to SPPs with almost 100% efficiency. With the increase in the metal film thickness the efficiency of the SPP excitation

decreases as the tunnelling distance increases. SPP on an interface between the prism and metal cannot be excited in this geometry as the wavevector of SPP at this interface is greater than the photon wavevector in the prism at all angles of incidence. To be able to excite SPP on the internal metal interface, an additional dielectric layer with a refractive index smaller that of the prism should be deposited between the prism and the metal film. In such a two-layer geometry, the photon tunnelling through this additional dielectric layer can provide resonant excitation of SPP on the inner interface. Thus, both SPP modes (on the surface and the interface) can be excited in such a configuration at different angles of illumination.

For thick metal films (or surfaces of bulk metal), for which the Kretschmann configuration cannot be used, SPP can be excited in the Otto configuration. Here, the prism where total internal reflection occurs is placed close to the metal surface, so that photon tunnelling occurs through the air gap between the prism and the surface. The resonant conditions are analogous to those in the Kretschmann configuration. This configuration is also preferable when direct contact with the metal surface is undesirable, e.g. for studying the surface quality.

7.3.2 Grating coupling

The mismatch in wavevector between the in-plane momentum $k_x = k \sin\theta$ of impinging photons and β can also be overcome by using diffraction effects at a grating pattern on the metal surface. For a one-dimensional grating of grooves with lattice constant a, as depicted in figure 180, phase-matching takes place whenever the condition

$$\beta = k \sin\theta \pm nG$$

is fulfilled, where $G = 2\pi/a$ is the reciprocal vector of the grating and $n = 1, 2, 3, \ldots$. As with prism coupling, excitation of SPPs is detected as a minimum in the reflected

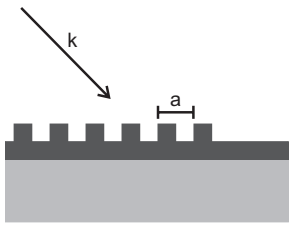

Figure 180: Grating coupling of a light with wave vector k impinging on a metal grating surface of period a.

light. The reverse process can also take place, when SPPs propagating along a modulated surface can couple to light and thus radiate (see figure 181).

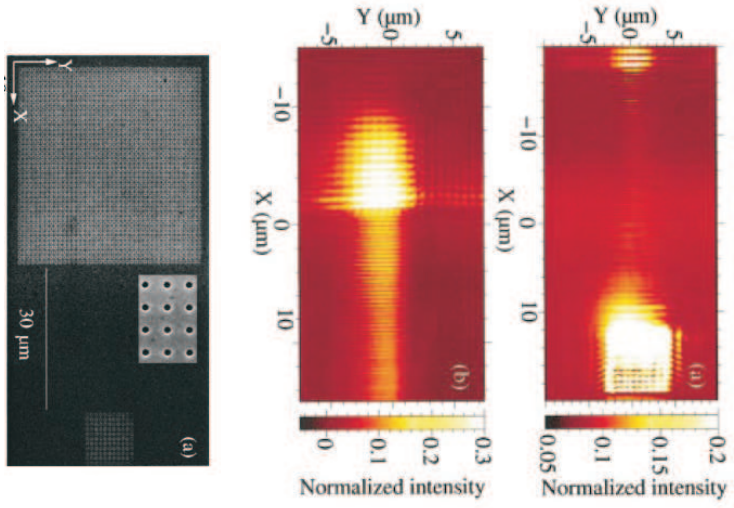

Figure 181: Left: SEM image of the pattern. 2 arrays with a period of 760 nm are separated by 30 mm. The hole diameter is 250 nm. The small array at the bottom is the source array whereas the big array at the top is not illuminated by the laser light and acts as a probe array. Inset: zoom in on the holes of one array.
Right: Near-field optical image of the pattern when the laser is focused on the small array and the electric field is along the x direction. [From Deveaux et al, APL 83, 4936 (2003)]

For one-dimensional gratings, significant changes to the SPP dispersion relations occur if the gratings are sufficiently deep so that the modulation can not longer be treated as a small perturbation. An SPP photonic bandgap is then formed when the period is equal to half the wavelength of the SPP. Just as for electron waves in crystalline solids, there are two SPP standing wave solutions, each with the same wavelength but, owing to their different field and surface charge distributions, they are of different frequencies (see figure 182(a)). The upper frequency solution ω_+ is of higher energy because of the greater distance between the surface charges and the greater distortion of the field. SPP modes with frequencies between the two band edges cannot propagate, and so this frequency interval is known as a stop gap.

7.3.3 Excitation using highly focused optical beams

As a variant of the prism coupling technique, a microscope objective of high numerical aperture can be used for SPP excitation. An oil immersion objective is

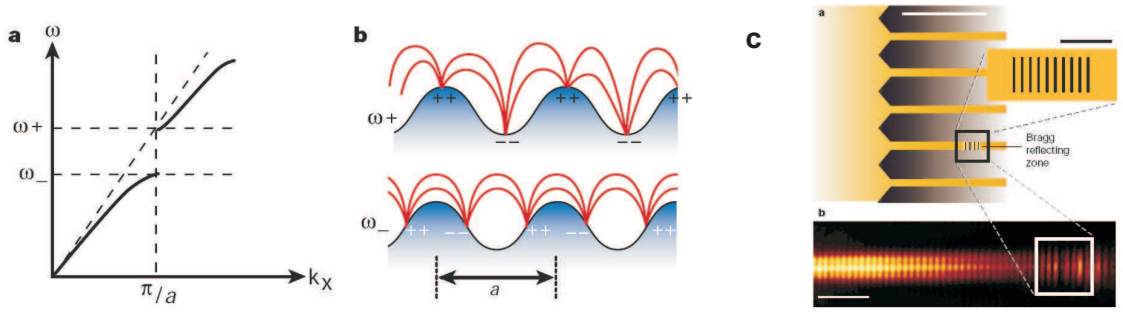

Figure 182: (a) SPP dispersion relation of a periodically modulated surface. (b) Schematic representation of the SPP modes near the band edges. (c) Realization of a SPP Bragg reflector. [From Barnes et al., Nature 424, 824 (2003).]

brought into contact with the glass substrate of a thin metal film via a layer of index matched immersion oil. The high N.A. of the objective ensures a large angular spread of the focused excitation beam, including angles $\theta > \theta_c$ greater than the critical angle for total internal reflection. In this way, wave vectors $k_x = \beta$ are available for phase-matching to SPPs at the metal/air interface. Off-axis entrance of the excitation beam can further ensure an intensity distribution preferentially around θ_{SPP} thus reducing the amount of directly transmitted/reflected light. The highly focused beam also allows for localized excitation within the diffraction limit. This scheme is especially convenient for the excitation of a continuum of SPPs at different frequencies. and the determination of their propagation lengths.

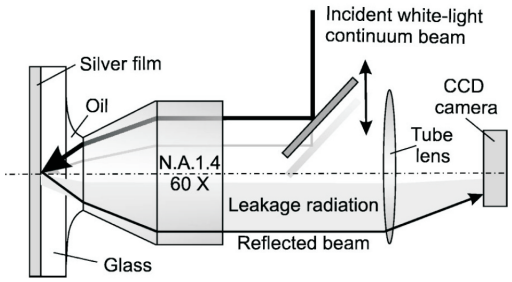

Figure 183: Schematic of the excitation of a white-light continuum of SPPs and their observation through an index-matched oil-immersion lens. [From Bouhelier and Wiederrecht, Opt. Lett. 30, 884 (2005)]

7.3.4 Near-field excitation

Near-field applications in SPP studies brought forth a new technique which provides the possibility to excite SPP locally with sub-wavelength resolution. Additionally, the effect of surface roughness on the SPP propagation and the scattering at individual surface defects can be studied with high spatial resolution.

Using illumination through a SNOM fiber tip, circular SPP waves can be locally launched at the surface. This configuration (see figure 184) can be treated as either a diffraction or tunnelling mechanism of the SPP excitation. In the former case, one can consider a near-field coupling of the light diffracted on the sub-wavelength aperture of the fiber tip in SPPs. In the latter case, because mainly the evanescent field components are generated at the aperture, one can describe the process as the photon tunnelling taking place from the fiber tip to the metal surface. This technique is somewhat analogous to the Otto configuration but allows local (with sub-wavelength precision) excitation of SPPs at the SNOM tip position.

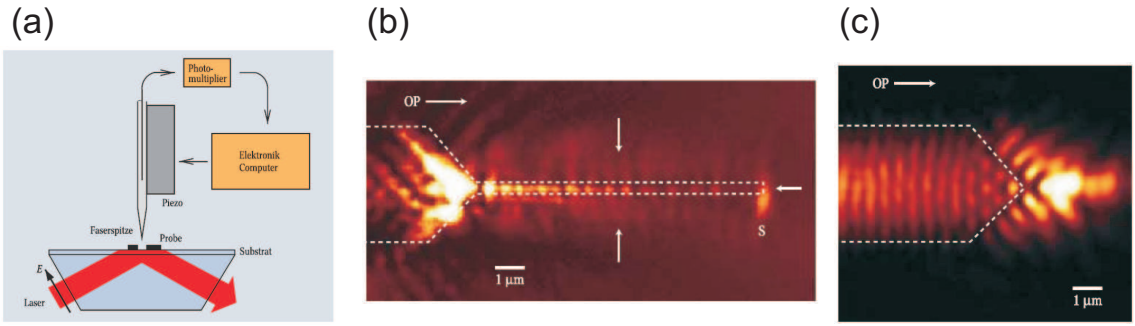

Figure 184: (a) Principle of the detection of SPPs (excited via the prism) with a SNOM probe. (b) and (c) SNOM images, propagation of SPPs along gold nanowires (wavelength 633 nm). [From Krenn and Aussenegg, Physik Journal 1 (2002) 39]

7.3.5 Coupling to integrated photonic elements

While the excitation schemes above are interesting for investigation of SPP propagation, practical applications of SPPs will require compact and efficient coupling schemes in integrated photonic circuits. Preferably, the plasmonic components should allow efficient matching with conventional dielectric waveguides and fibers.

One such coupling scheme is end-fire coupling, in which a free-space optical beam is focused on the end-facet of the desired waveguide. This scheme operates via matching the spatial field distribution of the waveguide as much as possible by

adjusting the beam width. This can be further miniaturized by directly connecting an optical fiber to the end-faced of the plasmon waveguide (see figure 185).

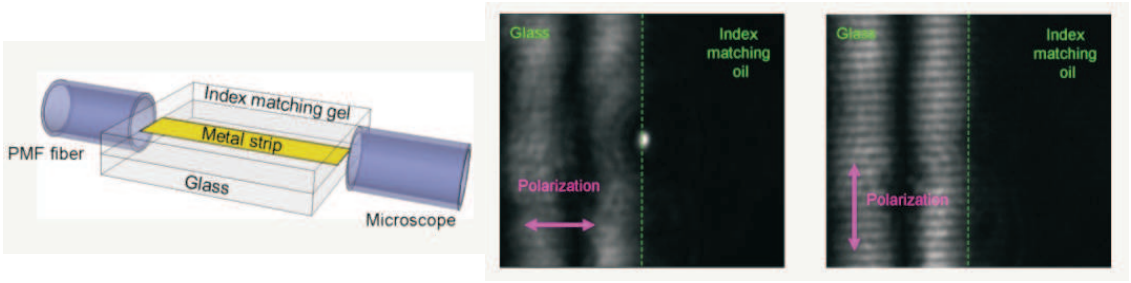

Figure 185: A polarization maintaining fiber coupled to a HeNe laser illuminates one end of the strip and the microscope collects the light scattered at the other end. The strip output lights up when the electric field is parallel to the short axis of the strip. This result is as expected because the SPP modes are mostly TM polarized. [From http://people.ee.duke.edu/˜drsmith/plasmon_waveguides.htm]

A convenient interfacing scheme makes use of optical fiber tapers brought into the immediate vicinity of the waveguide to achieve phase-matched power transfer via evanescent coupling (see figure 186). Fiber tapers are standard glass optical fibers that have been heated and stretched to a diameter that is at or below the wavelength of light, at which point the evanescent field of the guided mode extends into the surrounding air and allows the taper to function as a near-field optic. Similar approaches are used to couple light to microcavity structures such as microdisks.

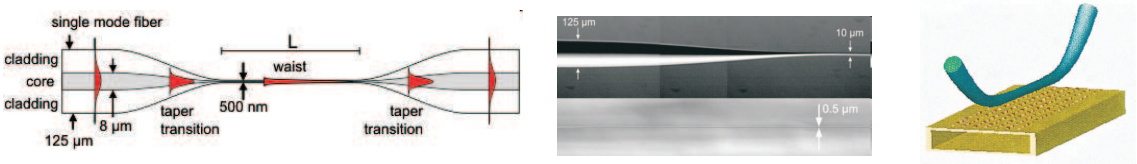

Figure 186: Left and center: Fiber tapers (D. Meschede, Univ. Bonn). Right: Fiber taper coupled to an SPP nanoparticle waveguide (Maier et al., APL 84, 3990 (2004).

7.4 Surface plasmon waveguides

In this subsection we discuss how to control the propagation of SPPs along waveguiding structures. The main figures of merit are here the confinement of SPPs to small dimensions and small losses.

7.4.1 Waveguides for long-range SPP modes

We have described before, that very thin metal films of thickness t, that are sandwiched between two symmetric layers of dielectric, interactions between SPPs on the bottom and top interfaces lead to the occurrence of coupled modes. The odd modes displays the interesting property of dramatically decreased attenuation with reduction in the metal thickness. Waveguides can be designed by defining metal stripes of lateral width w along which the SPPs propagate.

First we will consider the case $w, \lambda \gg t$. In figure 187, the dispersion relation for the propagation constant β and the attenuation α of such a metal stripe is given for the diverse existing modes. The symmetric modes are denoted by ss_b^0. One sees that the propagation constant dramatically decreases with reducing layer thickness. The long-range SPP modes can have show $1/e$ attenuation lengths up to the order of cm. This can by explained by the fact that only a small amount of the field resides in the thin metal layer, where Ohmic losses can occur. Instead the mode confinement increases to the order of the free-space wavelength into the dielectric. One thus has to find a compromise between small mode confinement and sub-wavelength guiding and, on the other hand, the minimization of losses.

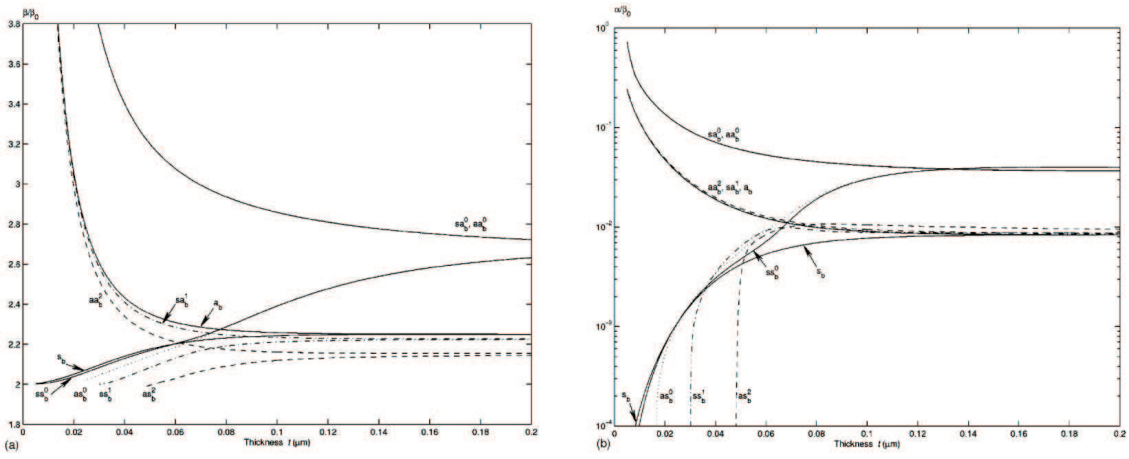

Figure 187: Dispersion relation for the propagation constant β and the attenuation α in a thin silver metal stripe of thickness t, width $w = 1\mu$m and infinite length, embedded in a dielectric with $\epsilon = 4$. The wavelength is 633 nm. The symmetric long-range SPP modes are denoted by ss_b^0. [From Berini, PRB 61, 10484 (2000)]

Figure 188 shows an example, of how such long-range SPP waveguides can be implemented to even design complex plasmon-optical elements, such as beamsplitters,

interferometers, or Bragg gratings.

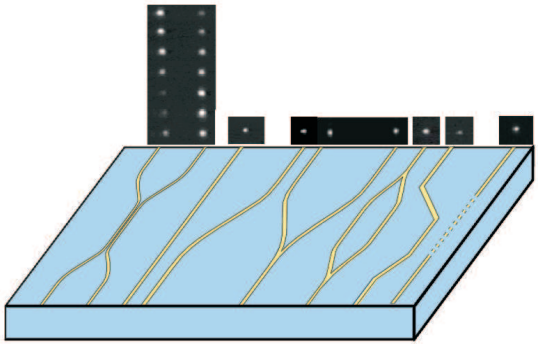

Figure 188: Waveguide structures for long-range SPPs. The gold stripes are 25 nm thick and have widths between 2–8 μm and are sandwiched between SiO_2 and a index-matching gel (both $\epsilon = 2.1$). The CCD images show the out-coupled light ($\lambda = 1550$ nm). [From Charbonneau et al., Opt. Expr. 3, 977 (2005)]

7.4.2 SPP guiding in metal nanowires

In contrast to the previous chapter, we now discuss the case of metal wires of small sizes in both dimensions, $w, t \ll \lambda$.

It is instructive to compare this with *dielectric* waveguides. In a dielectric waveguide with $\epsilon_{core} > 0$ and for propagation along z, the relation between propagation constant β, transverse wave vector components $k_{x,y}$ and frequency is

$$\beta^2 + k_x^2 + k_y^2 = \epsilon_{core} \frac{\omega^2}{c^2}$$

Since $\epsilon_{core} > 0$ and $k_{x,y}$ are real, this implies that $\beta, k_{x,y} \leq \sqrt{\epsilon_{core}}\omega/c = 2\pi n_{core}/\lambda_0$. According to the uncertainty relation between wave vector and spatial coordinates, the mode size is thus limited by the effective wavelength in the core medium,

$$d_x, d_y \geq \lambda_0/(2n_{core}) \tag{335}$$

However, if the guiding medium is a metal, then $\epsilon_{core} < 0$ and the transverse wave vectors $k_{x,y}$ must be imaginary. The guided waves are now one-dimensional. In this case, eq. (335) does not apply and the mode size can be substantially below the diffraction limit of the surrounding dielectric cladding.

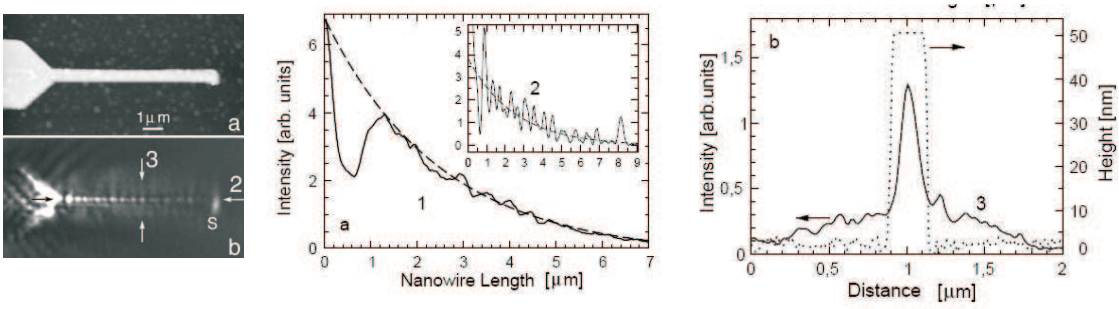

Figure 189: Left: topography (a) and near field intensity (b) of a gold nanowire (t = 50 nm, w = 200, λ_0 = 800 nm, length: 8 μm). The nanowire is addressed by a 3 m wide gold stripe, the SPP is propagating from left to right. The arrows indicate the positions of the cross-cuts in the graphs.
Center: cross-cut of the optical near-field intensity along the axis of the nanowire. Dashed line: exponential fit with $L = 2.5\mu$m.
Right: cross-cut of the optical near-field intensity perpendicular to the nanowire. The corresponding topography profile taken from a scanning electron microscope image is displayed by the dotted line. [From: Krenn et al., Europhys. Lett. 60, 663 (2002)]

As discussed in the previous section, the improved mode confinement goes along with increased Ohmic damping. An example for such a nanowire is given in figure 189. The longitudinal cross section of the near-field scan shows that indeed the propagation length is clearly smaller (several μm), than in the case of long-range SPPs, while the lateral cross section confirms the very strong confinement of the mode to the nanowire.

The propagation length in such systems can be drastically improved, however, when using chemically synthesized nanowires (CNW), instead of lithographically produced structures (LNW). In the latter case, the metal nanowires are produced by sputtering a gold film on a substrate and removing the spare parts using lithographic techniques. In this sputtering process produces a metal layer of poly-crystalline structure and shows some surface roughness that introduces further damping of the SPP by scattering. In contrast, CNWs can be fabricated with a well defined crystal structure, thereby minimizing surface plasmon damping due to scattering at roughness, domain boundaries, or defects.

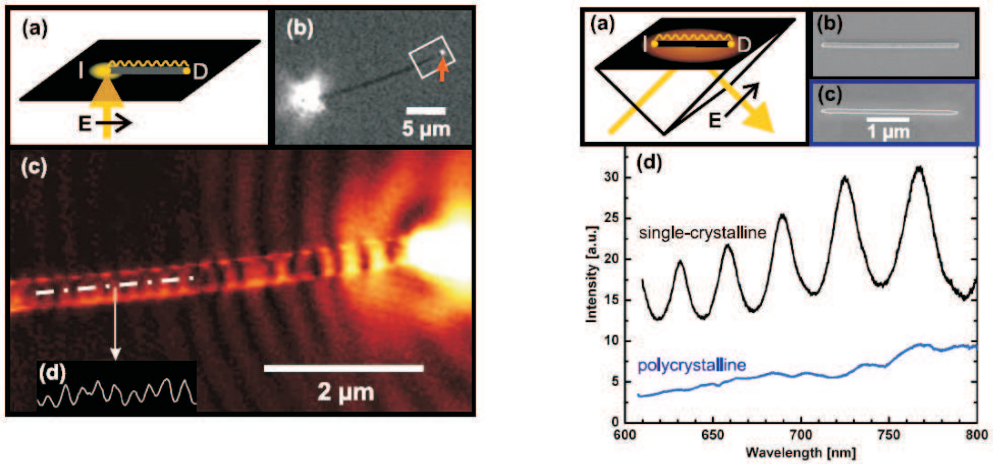

Figure 190: Left: (a) SPP propagation along the nanowire. I is input and D is distal end of the wire. (b) Microscopic image. The bright spot to the left is the focussed exciting light. The arrow indicates light scattered from the distal wire end. (c) SNOM image. (d) Cross-cut along the dotted line.
Right: Scattered light spectra of 3.3 μm silver nanowires, diameter 90 nm. (a) Sketch of optical excitation. The exciting light propagation direction projected onto the substrate plane is parallel to the nanowire axis, and the polarization is fixed in the plane of incidence. (b),(c) SEM images of a CNW and a LNW, respectively. (d) Scattered light spectra from the distal nanowire end facet of the CNW (single-crystalline) and the LNW (polycrystalline). [From Ditlbacher, et al, PRL 95, 257403 (2005)]

Figure 190 compares a CNW and a LNW (silver). The excited SPPs are expected to be reflected at the nanowire end facets and to form a standing wave. This can be indeed observed in the monocrystalline CNW, while the increased damping in the LNW hinders the formation of such standing waves.

7.4.3 Localized modes in gaps, grooves, and ridges

In the previous sections, we have discussed coupled SPP modes in dielectric/metal/dielectric structures. Similar modes can also occur in inverse geometries, i.e. metal/dielectric/metal structures. Here we discuss some possible realizations.

As shown in figure 191, different modes with orthogonal polarization are formed, that are either located inside the gap or at the edges of the metal layer, respectively. These modes have propagation lengths, in terms of power attenuation by $1/e$, in the range of 1 mm in the infrared, offering a low losses SPP guiding, similar to Long-Range-SPP modes, supported by thin metal stripes.

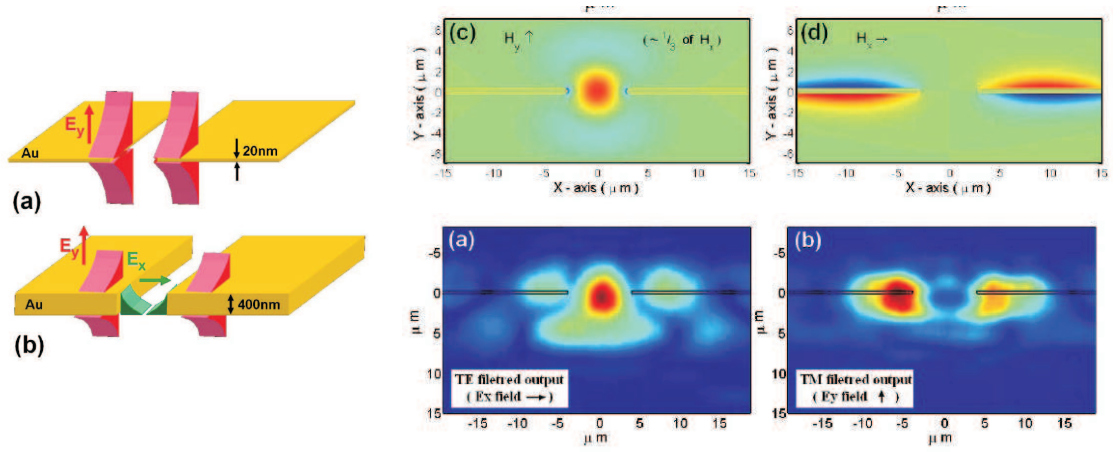

Figure 191: Modes in channel SPP waveguides. The structures are 400 nm gold layers on Si. The SPPs were excited at 1550 nm by end-fire coupling. The modal profile at the output facet were simulated (top images) and imaged through a high resolution objective onto a CCD camera (bottom images). [From Satubi and Orenstein, opt. Expr. 15, 4247 (2007)]

Similar modes can be defined by metal grooves and wedges. Examples of SPP propagation at $\lambda_0 = 1550$ nm are shown in figure 192 for different integrated plasmon-optical elements (beamsplitters, Mach-Zehnder interferometer, and ring interferometer). Depending on the groove width, the propagation lengths can be up to 100 μm or even longer, with the CPP field extending out of the groove.

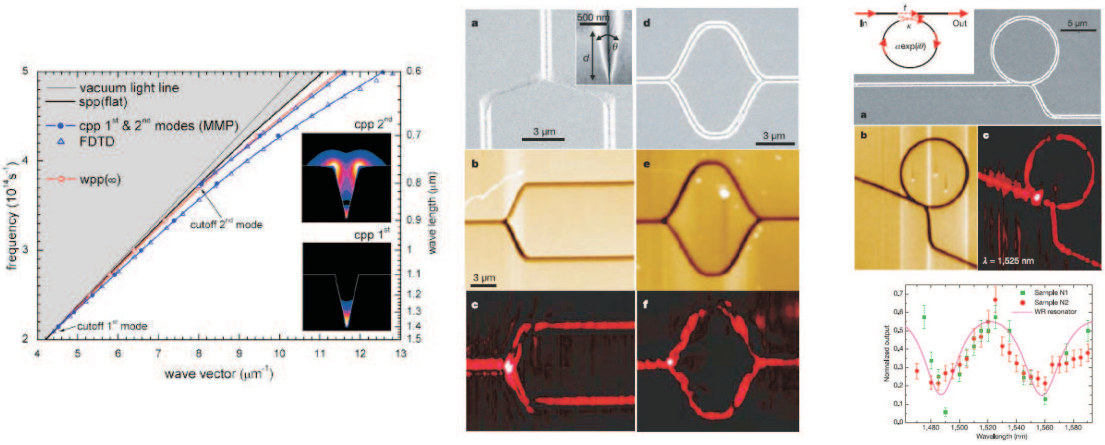

Figure 192: Left: dispersion relation and field distribution of different modes in groove SPP waveguides (from E. Moreno et al, Opt. Lett. 23, 3447 (2006)).
Center: Plasmonic Y-splitter and MachZehnder interferometer (from top to bottom: SEM, topographic, and near field images). Right: SPP ring resonator. (a) SEM, (b) topographical, (c) near-field image. Bottom graph: transmission spectra for two ring resonators. [From Bozhevolnyi et al., Nature 440, 508 (2006)]

An additional interesting feature of gap/groove waveguides is their lower susceptibility for losses at bent structures. While for the long-range SPP waveguides curvature radii of $\sim 100\mu$m or more are necessary (Berini and Lu, Opt. Exp. 14, 2365 (2006)), the radii used in figure 192 are on the order of 2 μm ($\approx 1.5\lambda$).

7.5 Localized plasmons on metal nanoparticles

Here we introduce another fundamental plasmonic excitation, *localized surface plasmons* (LSPs) (also known as *surface plasmons on metal nanoparticles*). LSPs are non-propagating plasmon excitations on metallic nanostructures.

For small isolated metal particles with sizes in the range of the penetration depth of an electromagnetic field (e.g. $\sim$ 20 nm for Ag in the optical range), the clear distinction between surface and bulk plasmon vanishes. An external field can penetrate into the volume and shift the conduction electrons with respect to the ion lattice (see figure 193).

The coherently shifted electrons together with the restoring field represent an oscillator, whose behaviour is defined by the effective electron mass, charge density and geometry of the particle. Most physical effects associated with LSPs can be ex-

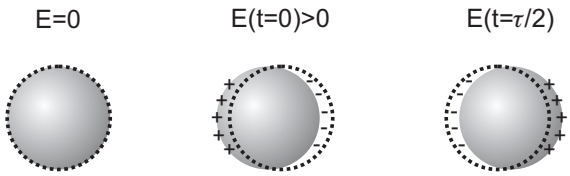

Figure 193: Localized surface plasmons on a metal nanoparticle in the absence (left) and presence (center & right) of an external electromagnetic field.

plained with this simple model. Spectrally the LSP resonances are in the visible to near infrared spectral regime. If excited at resonance, the amplitude of the induced electromagnetic field can exceed the exciting fields by a factor on the order of 10.

7.5.1 Plasmon resonance of a small spherical particle

Here we discuss in some more detail a LSP model in case of a small spherical particle. We assume a sphere of radius a in a uniform static electric field $\mathbf{E}_{in} = E_0\mathbf{e}_z$ The surrounding medium is isotropic and non-absorbing with dielectric constant ϵ_d, the metal sphere is described by a complex dielectric constat ϵ_s. We are interested in a solution of the Laplace equation $\Delta\Phi = 0$ from which we can obtain the electric field $\mathbf{E} = -\text{grad}\Phi$. In spherical coordinates, the Laplace equation is of the form

$$\frac{1}{r^2\sin\theta}\left[\sin\theta\,\partial_r(r^2\partial_r) + \partial_\theta(\sin\theta\,\partial_\theta) + \frac{1}{\sin\theta}\partial_\phi^2\right]\Phi(r,\theta,\phi) = 0$$

Due to the azimuthal symmetry, the general solution is independent of ϕ and has the form

$$\Phi_s(r,\theta) = \sum_{l=0}^{\infty} A_l r^l P_l(\cos\theta) \tag{336}$$

$$\Phi_d(r,\theta) = \sum_{l=0}^{\infty} (B_l r^l + C_l r^{-l-1}) P_l(\cos\theta) \tag{337}$$

where Φ_s is the potential inside the sphere and $\Phi_d = \Phi_{\text{scatter}} + \Phi_0$ the potential outside the sphere, consisting of an incoming and a scattered part.

When applying boundary conditions at the interface $r = a$ for tangential part of the electric field ($\partial_\theta\Phi_i = \text{const.}$, for $i = s, d$) and for the longitudinal part of the

displacement field ($\epsilon_i \partial_r \Phi_i = \text{const.}$), the potentials evaluate to

$$\Phi_s(r,\theta) = -\frac{3\epsilon_d}{\epsilon_s + 2\epsilon_d} E_0 r \cos\theta \tag{338}$$

$$\Phi_d(r,\theta) = -E_0 r\cos\theta + \frac{\epsilon_s - \epsilon_d}{\epsilon_s + 2\epsilon_d} E_0 \frac{a^3}{r^2}\cos\theta \tag{339}$$

$$= -E_0 r\cos\theta + \frac{\mathbf{p}\cdot\mathbf{r}}{4\pi\epsilon_0\epsilon_d r^3} \tag{340}$$

$$\text{with} \quad \mathbf{p} = 4\pi\epsilon_0\epsilon_d a^3 \frac{\epsilon_s - \epsilon_d}{\epsilon_s + 2\epsilon_d}\mathbf{E}_0 \tag{341}$$

Here we have introduced the dipole moment $\mathbf{p}$ that is induced in the sphere by the external field. The electric field can then be expressed as

$$\mathbf{E}_s = \frac{3\epsilon_d}{\epsilon_s + 2\epsilon_d}\mathbf{E}_0 \tag{342}$$

$$\mathbf{E}_d = \mathbf{E}_0 + \frac{1}{4\pi\epsilon_0\epsilon_d}\frac{3\mathbf{n}(\mathbf{n}\cdot\mathbf{p}) - \mathbf{p}}{r^3} \tag{343}$$

$\mathbf{n} = \mathbf{r}/r$ is the unit vector in direction of the point of interest.

The polarizability, defined by the relation $\mathbf{p} = \epsilon_0\epsilon_d\alpha\mathbf{E}_0$ then becomes

$$\alpha = 4\pi\epsilon_0 a^3 \frac{\epsilon_s - \epsilon_d}{\epsilon_s + 2\epsilon_d}$$

Note that this is of the same form as the Clausius-Mosotti equation. The scattering cross section of the sphere is then obtained by dividing the total radiated power of the dipole ($P = \omega^4/(12\pi\epsilon_0\epsilon_d c^3)|\mathbf{p}|^2$) by the intensity of the exciting wave ($I = (1/2)c\epsilon_0\epsilon_d E_0^2$):

$$\sigma_{\text{scatt}} = \frac{k^4}{6\pi\epsilon_0^2}|\alpha(\omega)|^2 \tag{344}$$

$$= \frac{8\pi}{3}k^4 a^6 \left|\frac{\epsilon_s - \epsilon_d}{\epsilon_s + 2\epsilon_d}\right|^2 \tag{345}$$

Figure 194 shows plots of the normalized scattering cross-section for silver and gold particles. A redshift of the resonance is observed by increasing the dielectric constant of the dielectric environment.

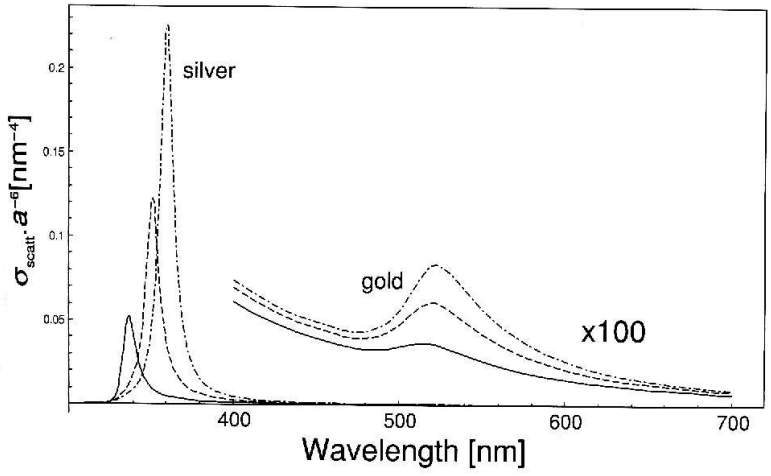

Figure 194: Plots of the scattering cross-section of spherical Ag and Au particles in different environments normalized by a^6 (a: particle radius). Solid line: vacuum, $n = 1$, dashed line: water, $n = 1.33$, dash-dotted line: glass, $n = 1.5$. [From Novotny and Hecht, "Principles of Nano-Optics", Cambridge Univ. Press 2006]

The power removed from the incident beam due to the plasmon is not only due to scattering but also due to absorption. The sum of absorption and scattering is called *extinction*. Using Poynting's theorem, we know that the power dissipated by a point dipole is $P_{\text{abs}} = (\omega/2)\text{Im}(\boldsymbol{\mu} \cdot \mathbf{E}_0^*)$. Using $\boldsymbol{\mu} = \epsilon_d \alpha \mathbf{E}_0$, the absorption cross section becomes

$$\sigma_{\text{abs}} = \frac{k}{\epsilon_0}\text{Im}(\alpha(\omega)) \tag{346}$$

$$= 4\pi k a^3 \text{Im}\left(\frac{\epsilon_s - \epsilon_d}{\epsilon_s + 2\epsilon_d}\right) \tag{347}$$

One sees that the scattering scales with a^6, while absorption process scale with a^3. Consequently, for large particles scattering dominates, whereas for smaller particles, extinction is dominated by absorption. The transition between the two regimes is characterized by a color change. For example small gold particles absorb green and blue and thus appear as red. On the other hand, large gold particles mostly scatter in the green and appear greenish. This effect is used in color glasses, as depicted in

the introduction of this chapter.

7.6 Applications of surface plasmons

7.6.1 Surface enhanced Raman scattering

An important application of surface plasmons is the enhancement of scattering of emitters near metal nanostructures. An example of this is Surface Enhance Raman Scattering (SERS)

The Raman effect describes the inelastic scattering between a photon and an emitter (e.g. a molecule) mediated by a vibrational or rotational mode of the emitter. Due to the energy exchange, the incoming photon of energy $\hbar\omega_L$ is shifted by the energy of the vibration $\hbar\omega_M$. If the photon looses energy, this is called Stokes scattering ($\omega_S = \omega_L - \omega_M$), if it gains energy by de-excitation of an vibrational mode it is called Anti-Stokes scattering ($\omega_{aS} = \omega_L + \omega_M$). This is symbolized in figure 195. In general the photons are not in resonance with the molecule but are excited to a virtual level.

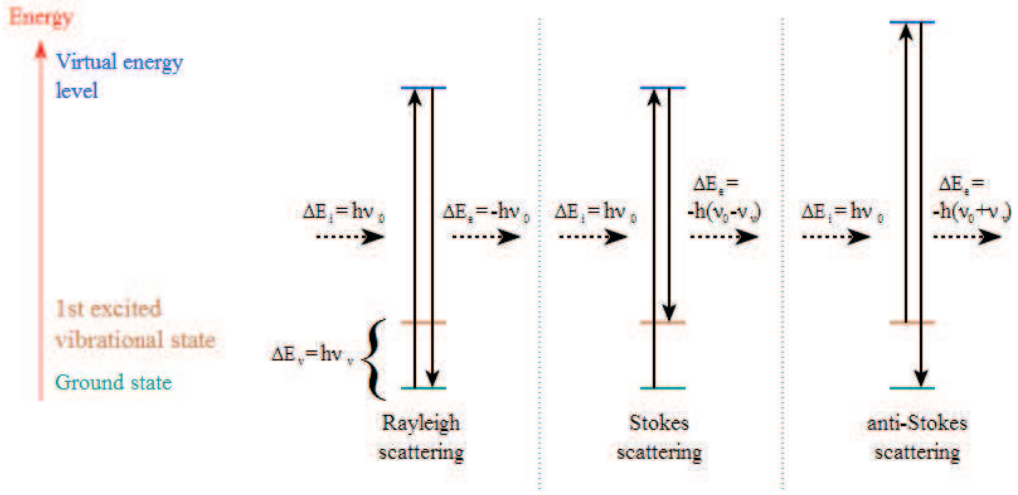

Figure 195: Schematics of the Raman scattering process.

Raman transitions can have very sharp lines and enable a detailed analysis of the molecule under study. Typically the Raman cross sections are more than 10 orders of magnitude smaller those of fluorescence processes ($\sigma_{\text{Raman}} \sim 10^{-31} - 10^{-29}$ cm^2/molecule).

SERS describes the enhancement of the Raman scattering by placing the molecule within the near-field of a metallic nanostructure (see figure 196) or a roughened metal surface. This enhancement is due to two effects: firstly, the Raman cross section is modified due to the changed environment. A much more important factor is the increased electromagnetic field due to excitations of LSPs and a crowding of the electric field lines (*lightning rod effect*) at the metal interface. The highest enhancements recorded to date are on the order of 10^{14}, achieved on roughened silver surfaces.

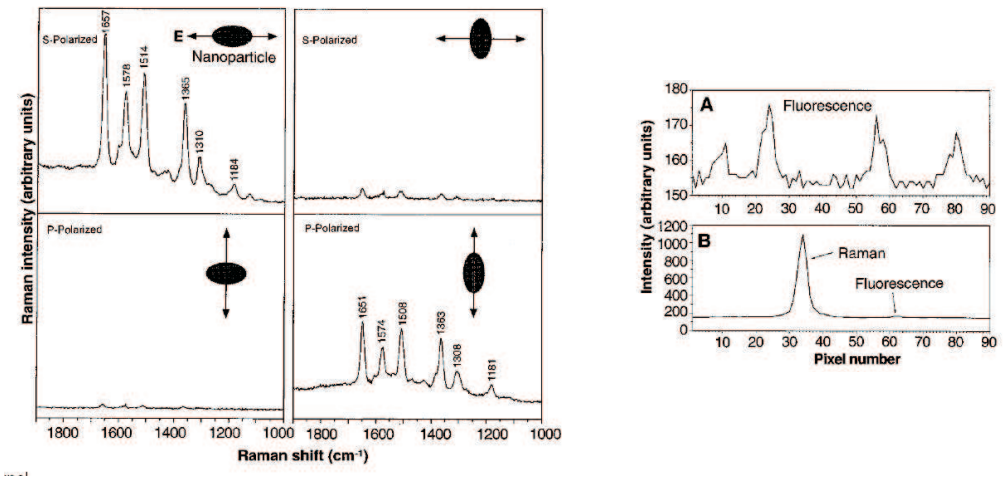

Figure 196: Left: SERS spectra of Rhodamine6G molecules on Ag nanoparticles (35 nm) with different orientation and polarization. Right: Comparison between the fluorescence and SERS signal. [From Nie et al, Science 275, 1102 (1997)]

7.6.2 Fluorescence enhancement

Similar to SERS, the fluorescence of an emitter in the proximity of metal nanostructures can be enhanced as well. Fluorescence here results from excitation of the emitter by the incident field, which can show significant enhancement due to plasmon resonances in the metal particle. However, care has to be taken, in order not to quench the fluorescence due to non-radiative processes, such as absorption by the surface plasmon resonance. This allows the utilization of metal nanostructures as nano-antennas.

Figure 197 shows an experiment, in which a diamond nanocrystal is placed near a gold nanoparticle or sandwiched between two particles. The intensity of the fluorescence could be thus enhanced by a factor of ~ 6, and the radiative decay rate was increased by a factor 6–9. The single-photon character of the emitter was conserved in this process.

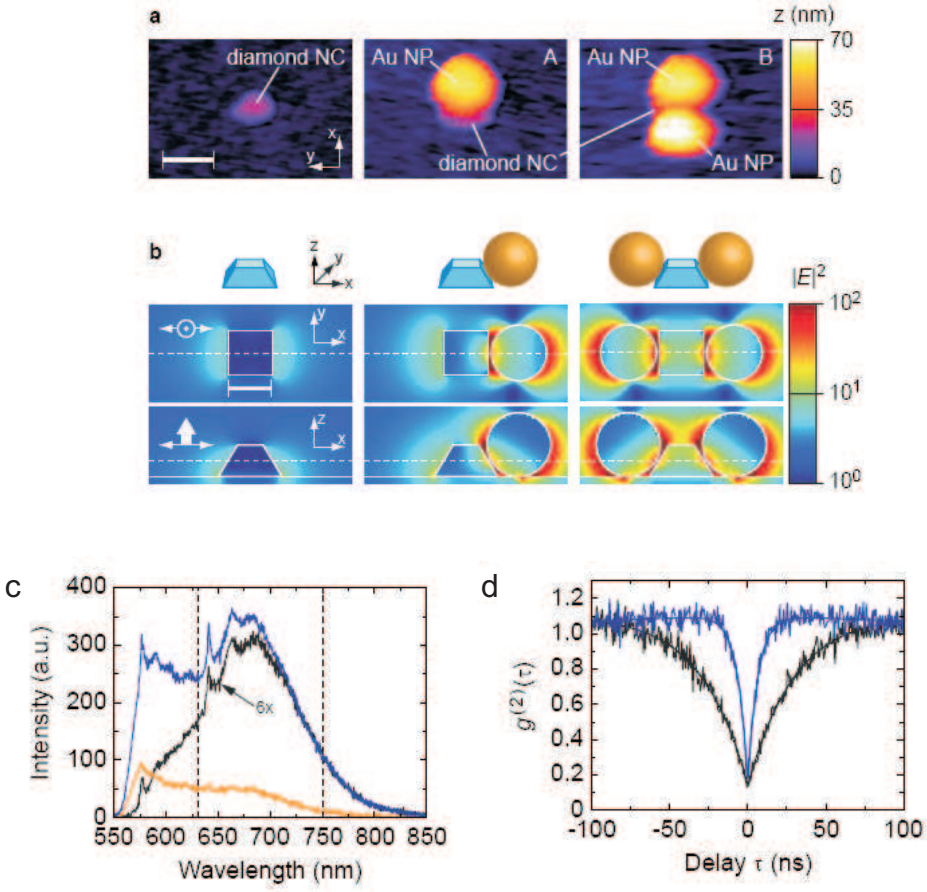

Figure 197: Fluorescence enhancement of a diamond nanocrystal (with nitrogen-vacancy defect center) near gold nanoparticles. (a) AFM images of three configurations: bare diamond, diamond near a Au particle, diamond between 2 Au particles. (b) Simulations of the intensity enhancement of the excitation light. (c) Fluorescence spectrum of the bare diamond (black, scaled by a factor of 6) and of configuration A under excitation parallel (blue) as well as perpendicular (orange) to the x axis at the same excitation intensity. (d) Normalized autocorrelation measurements on bare diamond (black) and configuration A (blue). [From Schietinger et al., Nano Lett. 9, 1694 (2009)]

Figure 198 shows another experiment, in which terrylene molecules are excited and a gold nanoparticle attached to a scanning probe tip is moved over the sample with variable distances. This nicely demonstrates the sensitivity to the distances when coupling emitters to metal nanoparticles.

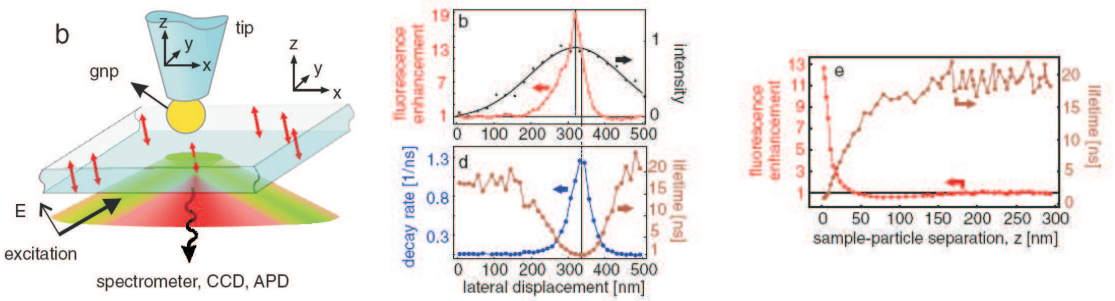

Figure 198: Left: Schematics of the experimental arrangement. Center: fluorescence enhancement (red), intensity (black), lifetime (brown), and decay rate (blue) as a function of the lateral position of the scanned gold particle (100 nm) 1 nm above the sample. Right: Fluorescence enhancement and lifetime as a function of the vertical displacement of the Au particle. [From Kühn et al, PRL 97, 017402 (2006)]

Finally, figure 199 shows an experiment in which not only the decay rate of a nanocrystal quantum dot (QD) is enhanced, but which also shows that the photons from a single emitter can excite single surface plasmons in a metallic nanowire (NW). These single SPPs then penetrated along the NW and eventually scatter at its distal end into freely propagating single-photons. The correlation measurements at either end of the NW and the cross-correlation measurement between the direct particle emission and the scattered plasmon emission demonstrates that SPPs indeed originate from the emitter and that they act as bosons which obey the same photon number statistics as light.

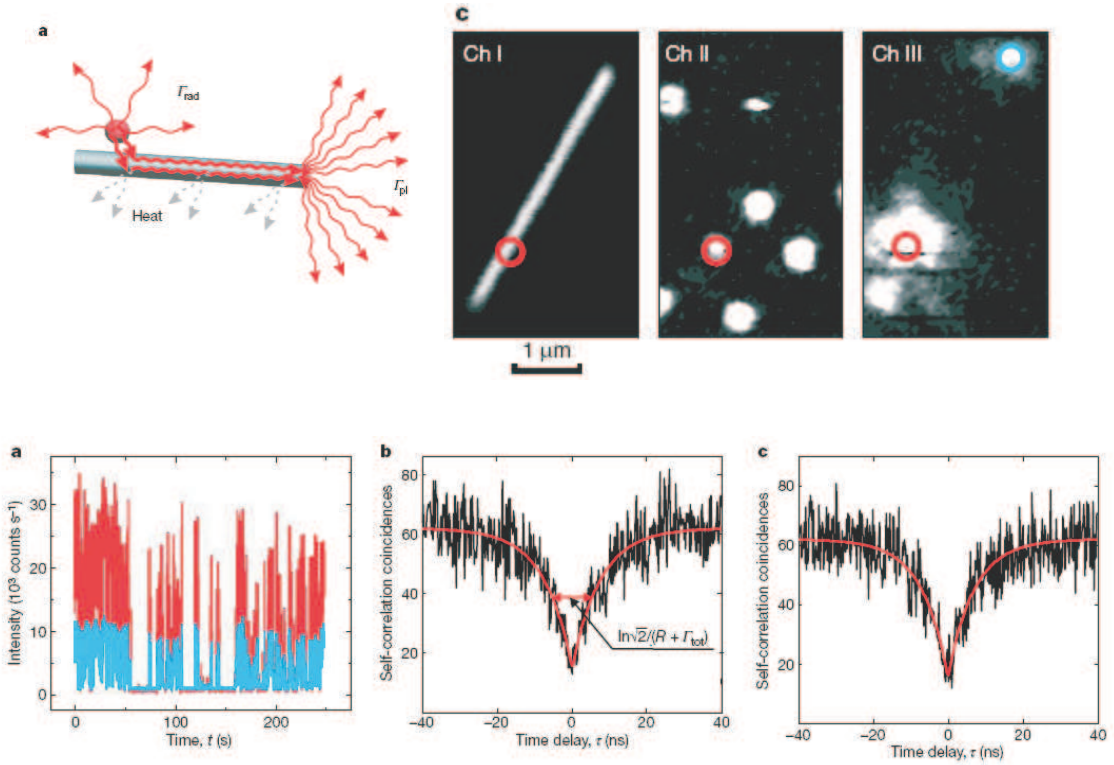

Figure 199: Top left: schematics of the experiment: a nanocrystal QD is placed next to a metal NW. Emission takes place in form of free photons as well as by exciting SPPs in the NW. Top right: μPL images of the system. I: nanowire image, II: image of QDs, III: the excitation laser was focused on the QD (red circle). The largest bright spot corresponds to the QD PL, while two smaller spots correspond to SPPs scattered from the NW ends. The blue circle indicates the farthest end of the nanowire, used for photon cross-correlation measurements. Bottom: (a) Time trace of PL counts (red curve) from a coupled QD and scattered light (blue) from the end of the coupled NW. Fluctuations are due to QD blinking. (b) Second-order correlation function of QD PL. The number of coincidences at $t = 0$ goes almost to zero, confirming that the QD is a single-photon source. (c) correlation function between fluorescence of the QD and scattering from the NW end, obtained by coincidences between channel II (QD) and channel III (NW end). [From Akimov et al., Nature 450, 402 (2007)]

7.6.3 Surface plasmon sensors in biology and medicine

Because the plasmonic interaction between metal nanoparticles is very sensitive to their separation and to the refractive index of the surrounding medium, they are used in biological, chemical, and medical sensing and detection applications.

The resonance shift due to a changing dielectric environment may allow for identifying different chemicals. In such an approach, a thin metal layer or surface containing a dense package of metal nanoparticles is prepared. When functionalizing the metal particles, they can be made sensitive to special types of bio-molecules. When the investigated chemical is rinsed over the surface, selective binding of species to the nanoparticles will change local dielectric properties resulting in a noticeable shift in LSP resonance (figure 200 right). Similarly, functionalized nanoparticles can be injected into cells and will bind to specific molecules, which can then efficiently be located (figure 200 left).

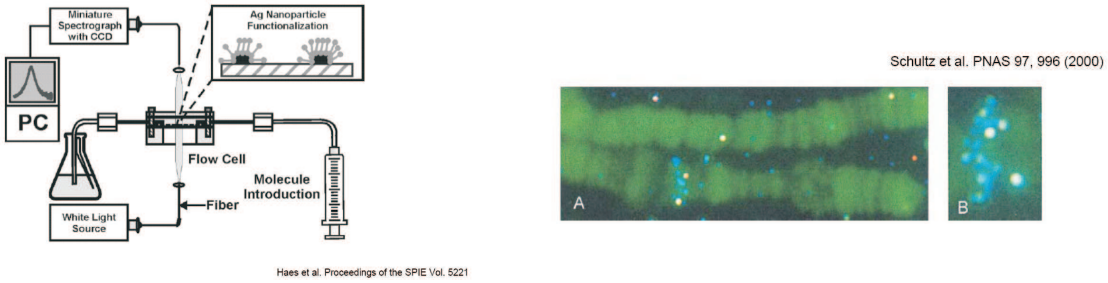

Figure 200: Left: sensing of bio-molecules by detecting the shift in LSP resonance. Right: specific binding of DNA coated nanoparticles to DNA can be used to locate certain complementary DNA sequences on chromosomes.

Because the plasmonic interaction between metal nanoparticles is very sensitive to their separation, precise measurements of the plasmon resonance wavelength of metal particle assemblies functionalized with biomolecules can be used as a molecular-scale ruler that operates over a length scale much larger than that in the fluorescence energy transfer metrology that is routinely used in biology. Practical applications of this concept in systems biology, such as imaging of the motion of molecular motors or of structural changes in proteins and in DNA (figure 201).

A final example for a potentially far-reaching application is the use of particles composed of a dielectric core and a metallic shell in cancer treatment. These particles, when injected into the human body, are selectively bound to malicious cells, whereupon laser irradiation at a precisely engineered plasmon resonance wavelength is

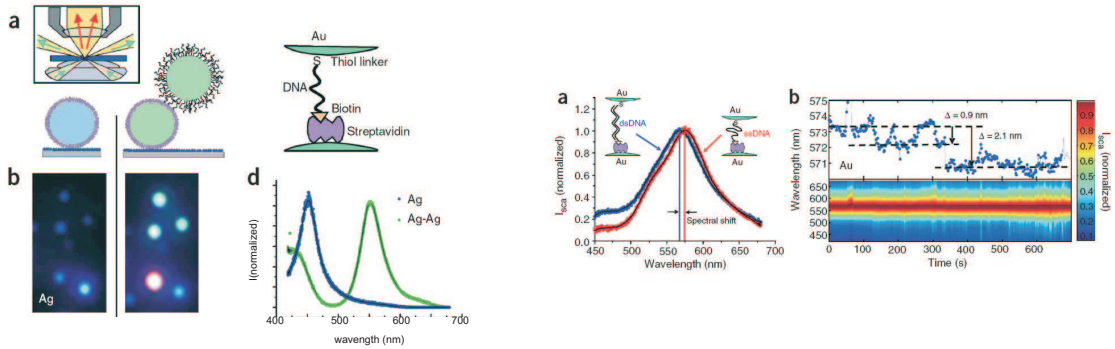

Figure 201: Single functionalized Ag nanoparticles as anchors for DNA molecules. When attaching a DNA molecule to two Au particles, the shift in resonance can be used to measure the distance between them (change from blue to blue-green). This allowed to study the dynamics of structural changes of the DNA molecule. [From Sönnichsen et al., Nature Biotech. 23, 741 (2005)]

used to heat the particles and thereby destroy the cells (Loo et al, Nano Lett. 5, 709 (2005)).